

Interpreting *Swift* and NuSTAR Observations of the Low-Luminosity Active Galactic Nucleus NGC 4278 with Radiatively Inefficient Accretion Flows and Implications for Neutrino Emission

ABHISHEK DAS ^{1,2}, QI FENG ³, ELEANOR YOUNG³, ASHWANI PANDEY ³, SHIGEO S. KIMURA ^{4,5} AND KOHTA MURASE ^{1,6,2,7}

¹*Department of Physics, The Pennsylvania State University, University Park, PA 16802, USA*

²*Institute for Gravitation and the Cosmos, The Pennsylvania State University, University Park, PA 16802, USA*

³*Department of Physics and Astronomy, University of Utah, Salt Lake City, UT 84112, USA*

⁴*Frontier Research Institute for Interdisciplinary Sciences, Tohoku University, Sendai 980-8578, Japan*

⁵*Astronomical Institute, Tohoku University, Sendai 980-8578, Japan*

⁶*Department of Astronomy & Astrophysics, The Pennsylvania State University, University Park, PA 16802, USA*

⁷*Center for Gravitational Physics and Quantum Information, Yukawa Institute for Theoretical Physics, Kyoto University, Kyoto 606-8502, Japan*

ABSTRACT

We report the first NuSTAR hard X-ray observations of the low-luminosity active galactic nucleus NGC 4278. The source is clearly detected beyond 10 keV with a hard X-ray spectrum consistent with a power law of photon index between 2.2 and 2.5 without evidence for a high-energy cutoff. The X-ray flux is low compared to the active state in 2021, but exhibits variability by a factor of ~ 2 on a timescale of a month. We discuss the origin of the hard X-ray emission and explore its connection to gamma rays and high-energy neutrinos. We explain the X-ray data, including both quiescent and active states, using a radiatively inefficient accretion flow (RIAF) model with a variable accretion rate. We also show that TeV gamma rays cannot escape from the RIAF disk, and very high-energy gamma rays observed in LHAASO are likely to originate from outer regions such as jets and winds, which is consistent with our results favoring a magnetically arrested disk. We also discuss hidden neutrino emission from RIAFs together with possible connections to coronae of active galactic nuclei with standard, radiatively efficient disks.

Keywords: High energy astrophysics (739) — Low luminosity active galactic nuclei (2033) — LINER galaxies (925) — X-ray astronomy (1810) — Accretion (14) — Gamma-ray astronomy (628)

1. INTRODUCTION

Ground-based gamma-ray observatories have discovered more than 200 sources of TeV gamma-ray radiation, which can only be produced in some of the most extreme environments in the Universe. New types of TeV gamma-ray sources are still being discovered, e.g., recurring novae (H. E. S. S. Collaboration et al. 2022). Ground-based water Cherenkov telescopes, such as LHAASO and HAWC, have the unique advantage of

a large field of view (FoV) and a high duty cycle (not affected by the Sun or the Moon) for discoveries of new TeV sources.

The first catalog of the highest-energy (from 1 TeV to above 100 TeV) gamma-ray sources detected by LHAASO (Cao et al. 2024a) includes 32 new TeV sources. Only one of these sources was identified by the LHAASO Collaboration as a candidate extragalactic source, 1LHAASO J1219+2915, which is coincident with the low-luminosity active galactic nucleus (LLAGN) NGC4278. It was only detected by the WCDA (1–25 TeV) of LHAASO at a statistical significance of $\sim 7\sigma$, with a power-law index of 2.67 ± 0.17 and as a point source (the 95% UL on its 30% containment radius is 0.08°). Subsequently, LHAASO reported a ~ 5 -month period when NGC 4278 exhibited an active state with

Corresponding author: Abhishek Das
ajd6518@psu.edu

Corresponding author: Qi Feng
qi.feng@utah.edu

elevated TeV gamma-ray flux, between August 23, 2021, and January 10, 2022 (Cao et al. 2024b).

NGC 4278 is a nearby ($z = 0.0021$) low-ionization nuclear emission-line region (LINER)/LLAGN at a luminosity distance of 16.7 Mpc, exhibiting a two-sided parsec-scale ‘‘S-shaped’’ jet structure from radio observations (Giroletti et al. 2005; Tremblay et al. 2016). The radio jets in the north and south directions show asymmetry in their apparent velocity, which can be explained by either a mildly relativistic jet ($\beta \sim 0.75$) at a small viewing angle (2° – 4°) or jets at larger viewing angle strongly interacting with the surrounding medium (Giroletti et al. 2005). An intriguing transient GeV gamma-ray source 1FLT J1219+2907, spatially coincident with NGC 4278, was detected at $\sim 5\sigma$ by *Fermi*-LAT in 2009 between March 5 and April 5, with a 95% error radius of 0.5° (Baldini et al. 2021). In the X-ray band, NGC 4278 has been observed by XMM-Newton in 2004 and Chandra between 2005 and 2010, revealing X-ray flux variability on timescales of years (Pellegrini et al. 2012) and months (Younes, G. et al. 2010). Evidence for flux variation by $\sim 10\%$ on timescales of hours has also been reported Younes, G. et al. (2010). The source has not been observed in X-ray after 2010, except for a short *Swift* observation (~ 0.9 ks exposure) in 2021.

In this work, we describe the first NuSTAR observations of NGC 4278, the measured X-ray spectrum beyond 10 keV, and its variability; we interpret the X-ray results using a radiatively inefficient accretion flow model; we also discuss the possible association between the X-ray emission and the observed TeV gamma rays, as well as the hypothetical neutrinos.

2. OBSERVATIONS AND DATA ANALYSIS

2.1. NuSTAR

The Nuclear Spectroscopic Telescope Array (NuSTAR) uses two co-aligned grazing incidence telescopes with two independent focal plane modules (FPMA and FPMB) to detect hard X-rays between 3 and 79 keV (Harrison et al. 2013). NuSTAR covers a $13' \times 13'$ FoV and achieves an on-axis point spread function of $18''$ (Harrison et al. 2013).

NuSTAR observed NGC 4278 for the first time on December 6, 2024, for ~ 43.1 ks (observation ID 61002012002). Subsequently, NuSTAR observed the source again on January 13, 2025, for ~ 45.7 ks (observation ID 61002012004).

The NuSTAR data were analyzed using standard software (NuSTARDAS) as part of HEASOFT. An absorbed power-law model with a cross-normalization parameter was used to simultaneously fit the spectrum from each of

the two observations. The total Galactic neutral hydrogen column density is $N_H = 2.22 \times 10^{20}$ atoms cm^{-2} toward the direction of NGC 4278 (Willingale et al. 2013). We performed the fit to the X-ray spectra with both N_H free and N_H fixed at the Galactic value.

2.2. Swift

The X-Ray Telescope (XRT) on the Neil Gehrels *Swift* Observatory is capable of detecting X-rays from ~ 0.3 keV to 10 keV (Gehrels et al. 2004; Burrows et al. 2005).

Previously, *Swift*-XRT observed the vicinity of NGC 4278 two times, including a 923-s exposure on November 28, 2021 (observation ID 03109562002), during the LHAASO-reported active state. Following the announcement of a TeV gamma-ray detection by LHAASO, *Swift* performed 10 observations of NGC 4278 between May 2024 and January 2025. These more recent observations include a 1584-s exposure on January 13, 2025, taken on the same day as one of the two NuSTAR observations.

The *Swift*-XRT data were analyzed following the standard procedure using HEASOFT and modeled using an absorbed power law. A joint fit with both *Swift*-XRT and NuSTAR data taken on January 13, 2025, was also performed.

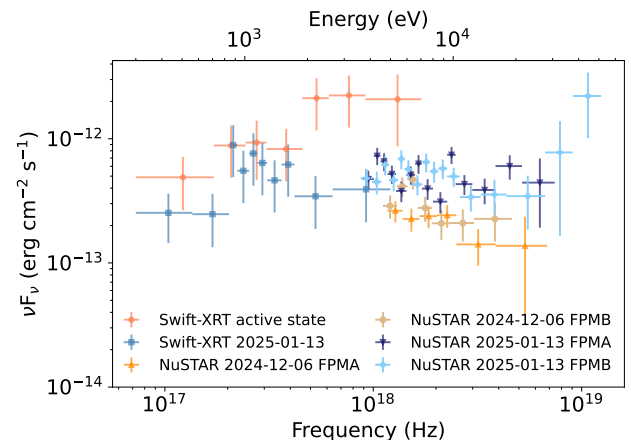


Figure 1. The X-ray spectra of NGC 4278. Quasi-simultaneous spectra measured by *Swift*-XRT (blue squares) and NuSTAR (dark blue down triangles for FPMA and light blue plus signs for FPMB) on January 13, 2025, show a moderate flux level. The *Swift*-XRT spectrum measured during the LHAASO-reported active state (pink circles) shows an X-ray active state that is more prominent above 2 keV. The NuSTAR spectrum (orange up triangles for FPMA and gold cross signs for FPMB) measured on December 6, 2024, shows a low-flux state. The flux points are corrected for the Galactic neutral hydrogen absorption.

Table 1. Best-fit parameters of absorbed power-law models for the *Swift*-XRT and NuSTAR X-ray spectrum measured on January 13, 2025.

Parameter	Best-Fit Value and 1σ Uncertainty	
	N_H fixed	N_H free
Index	2.02 ± 0.05	2.25 ± 0.07
Normalization ($10^{-4} \text{keV}^{-1} \text{cm}^{-2}$)	3.2 ± 0.3	5.0 ± 0.6
N_H ($10^{20} \text{atoms cm}^{-2}$)	2.22	24.9 ± 7.7
χ^2/DOF	125.6/89	104.1/88

3. RESULTS

3.1. X-ray spectrum

Fig. 1 shows the X-ray spectrum measured quasi-simultaneously by *Swift*-XRT and NuSTAR on January 13, 2025. The *Swift*-XRT spectrum measured on November 28, 2021, during the LHAASO-reported active state, as well as the first NuSTAR spectrum measured on December 6, 2024, are shown for comparison.

The X-ray spectrum measured by *Swift*-XRT during the active state was hard, with a power-law photon index of 1.4 ± 0.3 , suggesting that the synchrotron emission in the spectral energy distribution (SED) continues to rise beyond a few keV. The active-state X-ray spectrum shows a much larger increase in the flux above 2 keV compared to the flux below 2 keV (see Fig. 1).

The recent NuSTAR observations measured an almost flat X-ray spectrum without any sign of a high-energy cutoff. The two NuSTAR observations showed that the 3-30 keV X-ray spectrum became marginally harder, with the power-law photon index changing from 2.5 ± 0.2 on December 6, 2024, to 2.2 ± 0.1 on January 13, 2025 (N_H fixed at the Galactic value).

The measured X-ray spectrum is curved toward low energies after correcting for the Galactic neutral hydrogen absorption. This suggests either an intrinsic curvature, or the existence of additional absorption beyond the Galactic neutral hydrogen if the intrinsic spectrum follows a power law from 0.3 keV to a few tens of keV. The joint *Swift*-XRT and NuSTAR X-ray spectra measured on January 13, 2025, are fitted to an absorbed power-law model (`tbabs*po`) with the neutral hydrogen column density either fixed to the Galactic value or left free (see Table 1). A simple F -test shows that leaving N_H free significantly improves the power-law fit at a p -value of 5×10^{-5} (or $\sim 4\sigma$). Although the curvature can also be intrinsic and could be explained by a radiatively inefficient accretion flow (see Section 4.1).

A relativistic reflection disk-corona model has been tested on the X-ray spectrum; however, due to limited statistics, the parameters are not well constrained.

It is worth noting that the NuSTAR spectrum measured on January 13, 2025, becomes background-dominated above 20 keV, and the flux measurements in the two high-energy bins above 30 keV from FPMB are not statistically significant (light blue pluses in Fig. 1).

3.2. X-ray flux variability

Despite the sparsity of X-ray monitoring before 2024, the serendipitous *Swift*-XRT observation during the LHAASO-reported “active” state on November 28, 2021 captured an elevated 0.3-10 keV X-ray flux of $(6.2 \pm 1.8) \times 10^{-12} \text{erg cm}^{-2} \text{s}^{-1}$, as shown in Fig. 2 (*top*).

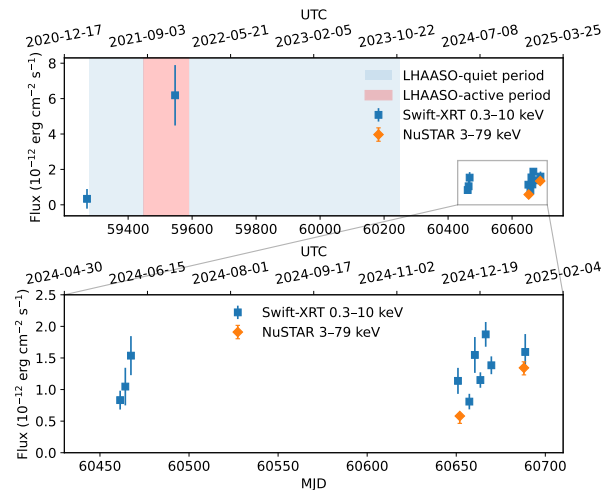


Figure 2. (*Top*) The X-ray light curve of NGC 4278 between 2020 and 2025, showing an active X-ray flux state during the LHAASO-reported active periods. (*Bottom*) A zoomed-in view of the variability during the X-ray campaign in 2024 and 2025, showing a low to moderate flux state with variability by a factor of ~ 2 over timescales of weeks to months.

The 10 recent *Swift*-XRT observations between May 2024 and January 2025 showed a much lower 0.3-10 keV X-ray flux, with a mean and standard deviation of $(1.29 \pm 0.35) \times 10^{-12} \text{erg cm}^{-2} \text{s}^{-1}$, as shown in Fig. 2 (*bottom*). Comparing the low and high X-ray fluxes, the *Swift*-XRT measured 0.3-10 keV flux during the 2021 gamma-ray active period likely corresponds to an X-ray active state, showing a higher flux by a factor of ~ 5 with a statistical significance of $\sim 2.7\sigma$.

Although the X-ray flux was lower during the 2024 – 2025 campaign, it was still variable on timescales of days to months. A constant fit to the low-state 0.3-10 keV flux yielded a $\chi^2 = 34.56$ over 9 degrees of freedom,

corresponding to a p -value of $\sim 7 \times 10^{-5}$, suggesting variability was observed over a few months. The 0.3-10 keV flux increased by almost a factor of 2 from December 2024 to January 2025. The fractional variability Vaughan et al. (2003) from the 10 low-state XRT observations is 0.21 ± 0.06 .

The two NuSTAR observations also showed a factor of ~ 2 increase in the 3-79 keV hard X-ray flux, from $(5.8_{-1.2}^{+1.0}) \times 10^{-13} \text{ erg cm}^{-2} \text{ s}^{-1}$ on December 6, 2024, to $(1.4 \pm 0.1) \times 10^{-12} \text{ erg cm}^{-2} \text{ s}^{-1}$ on January 13, 2025. We therefore refer to the NuSTAR observation on December 6, 2024, as the “quiescent” flux state, and that on January 13, 2025, as the “moderate” flux state.

3.3. Broadband SED

Fig. 3 shows the broadband SED of NGC 4278 during the quiescent and moderate X-ray flux states in 2024 and 2025, together with the soft X-ray SED during the active state in 2021, as well as the archival SEDs across many wavelengths. The TeV gamma-ray spectra measured by LHAASO (Cao et al. 2024b) during the active state (April 10, 2021 – August 28, 2021) and the quiet state (March 5, 2021 – October 31, 2023, excluding the active period) are shown. NGC 4278 is nominally not detected by *Fermi*-LAT, but Bronzini et al. (2024) reported a 4.3σ detection in an analysis of the *Fermi*-LAT data between March 2021 to October 2022. We adapted the *Fermi*-LAT spectrum during the active

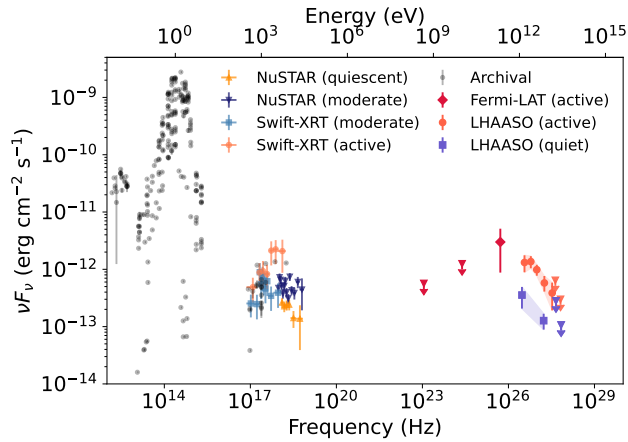


Figure 3. The broadband SED of NGC 4278. The active state SED is measured by *Swift*-XRT (pink circles), *Fermi*-LAT (red diamonds) (Bronzini et al. 2024), and LHAASO (tomato red circles) (Cao et al. 2024b). The “quiescent” NuSTAR SED was measured on December 6, 2024. The “moderate” X-ray SED was measured quasi-simultaneously by *Swift*-XRT and NuSTAR on January 13, 2025 (see Sec. 3.1 and 3.2). The archival SEDs are taken from the ASI Space Science Data Center (SSDC) SED Builder (Stratta et al. 2011).

state of the source from Bronzini et al. (2024). The archival SEDs are taken from the ASI Space Science Data Center (SSDC) SED Builder⁸ (Stratta et al. 2011). The archival data shown are from multiwavelength surveys from radio to X-ray energies (Boller et al. 2016; Voges et al. 1999; Wright et al. 2010; Moshir & et al. 1990; Joint Iras Science 1994; Condon et al. 1998; Gregory et al. 1996; White et al. 1997; White & Becker 1992; Dixon 1970; Myers et al. 2003; Jackson et al. 2007; Healey et al. 2007).

4. THEORETICAL MODELING OF SEDS

4.1. RIAF Model

We attempt to explain the SED with a radiatively inefficient accretion flow (RIAF) model, where thermal electrons emit multi-wavelength photons via synchrotron and Comptonization processes (Narayan & Yi 1994; Blandford & Begelman 1999; Mahadevan 1997; Pesce et al. 2021). Such a model explains keV-MeV photons without the need for a big blue bump, which is typically absent in LLAGNs. The model is characterized primarily by three parameters: the viscosity parameter, α , the pressure ratio of gas to magnetic fields, β , and the normalized accretion rate, \dot{m} , which is related to the accretion rate \dot{M} as $\dot{m} = \dot{M}c^2/L_{\text{Edd}}$. We also define the normalized radius $\mathcal{R} = R/R_S$. The radial velocity, number density, proton thermal temperature, magnetic field, Thomson optical depth, and Alfvén velocity for the RIAF model are defined and analytically approximated as follows (Kimura et al. 2019a; Kimura et al. 2021):

$$V_R = \alpha V_K/2 \simeq 3.4 \times 10^8 \mathcal{R}_1^{-1/2} \alpha_{-1} \text{ cm/s}, \quad (1)$$

$$n_p = \frac{\dot{M}}{4\pi m_p R H V_R} \simeq 1.5 \times 10^7 \mathcal{R}_1^{-3/2} \alpha_{-1}^{-1} M_{8.5}^{-1} \dot{m}_{-3} \text{ cm}^{-3}, \quad (2)$$

$$k_B T_p \simeq \frac{GMm_p}{4R} \simeq 12 \mathcal{R}_1^{-1} \text{ MeV}, \quad (3)$$

$$B = \sqrt{\frac{8\pi n_p k_B T_p}{\beta}} \simeq 84 \mathcal{R}_1^{-5/4} \alpha_{-1}^{-1/2} M_{8.5}^{-1/2} \dot{m}_{-3}^{1/2} \beta^{-1/2} \text{ G}, \quad (4)$$

$$\tau_T \simeq n_p \sigma_T R \simeq 9.0 \times 10^{-3} \mathcal{R}_1^{-1/2} \dot{m}_{-3} \alpha_{-1}^{-1}, \quad (5)$$

$$\beta_A = \frac{B}{\sqrt{4\pi n_p m_p c^2}} \simeq 0.16 \mathcal{R}_1^{-1/2} \beta^{-1/2}, \quad (6)$$

where $V_K = \sqrt{GM/R}$ is the Keplerian velocity, $H \simeq R/2$ is the scale height, and $A_n = A/10^n$.

⁸ ASI Space Science Data Center (SSDC) SED Builder: <https://tools.ssdsc.asi.it/SED/>

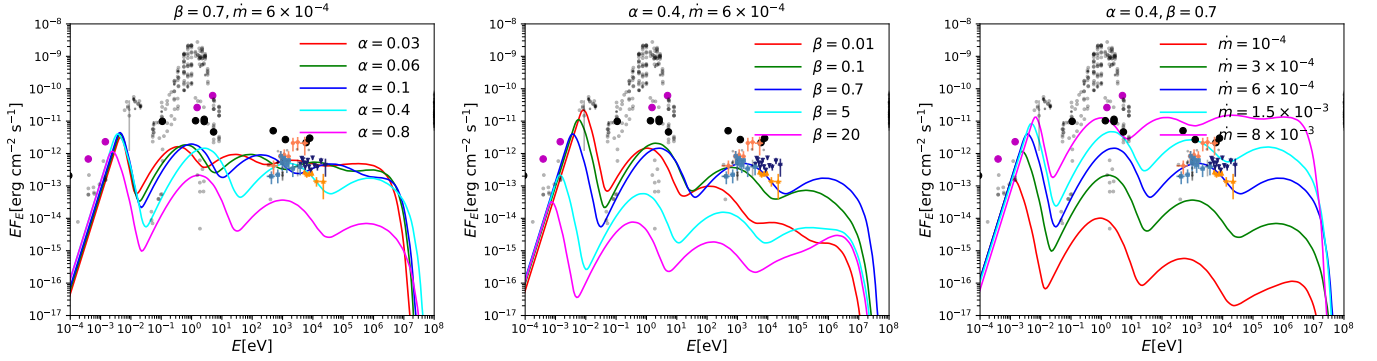


Figure 4. Left: SEDs with varying α for constant values of β and \dot{m} . Middle: Same with β for constant values of α and \dot{m} . Right: Same with \dot{m} for constant values of α and β . The archival and X-ray data points have the same legends as fig. 3. The purple and black data points are from Nemmen et al. (2014) and Bandyopadhyay et al. (2019) respectively.

The bolometric luminosity of the SED is computed with given physical quantities in RIAFs, such as density, magnetic field, and electron temperature. We obtain the electron temperature by balancing the heating and cooling rates in the RIAF (e.g., Kimura et al. 2021). For the heating rate, we assume that half of the released gravitational energy is used for heating the plasma, and electrons receive f_e of the released energy, i.e., the electron heating rate is given by $Q_e \approx f_e \dot{M} c^2 / (2R)$. We use the fitting formula given by Chael et al. (2018) for f_e . For cooling processes, we consider advection and radiative cooling. For radiative cooling, we take into account synchrotron, Comptonization, and bremsstrahlung processes (see Kimura et al. 2015 for details). First, we compute the electron temperature, $T_{e,\text{rad}}$, by balancing radiation cooling and heating. If advection cooling is dominant, the temperature should be set to $T_{e,\text{adv}} = f_e T_p$. We use the lower electron temperature, $T_e = \min(T_{e,\text{adv}}, T_{e,\text{rad}})$, to calculate the multi-wavelength spectrum.

In Fig. 4, we demonstrate the effects of varying each of the three main parameters. The left panel demonstrates the effect of different values of α on the SED for a constant β and \dot{m} . We can see that for $\alpha \in [0.03, 0.4]$, lowering the viscosity parameter α increases the ‘‘Compton Y parameter’’ corresponding to a stronger Comptonization process, where photons on average gain more energy. The black hole mass of NGC 4278 is set to $3 \times 10^8 M_\odot$ (Wang & Zhang 2003). Because of efficient Comptonization, the electron temperature in RIAF decreases, and thus, single scattering does not increase the photon energy significantly, but increases the optical depth, causing efficient multiple scatterings, resulting in significant increase of Comptonization photons. The middle panel shows the effect of varying β for constant α and \dot{m} . On the other hand, a lower plasma β results in a lower electron temperature because of efficient synchrotron cooling, thereby decreasing the Y parameter

and causing inefficient Comptonization. Finally, the last panel demonstrates the effect of \dot{m} on the SED. More accretion results in increased Comptonization because of higher values of the Y parameter, resulting in greater flux at higher energies.

We present our results assuming a single emission zone. We show that the single-zone modeling is sufficient. For the multi-zone scenario, we consider three concentric emission regions with radii, the smallest radius being $10R_S$. The parameters α and β are assigned to be constant across each emission region and behave exactly as they do in the single-zone scenario, while \dot{m} at different radii is calculated as follows:

$$\dot{m}[i] = \dot{m} \times (R[i]/R[0])^s$$

where $i = 0, 1, 2, \dots$ is an index assigned to each concentric emission region, R is the emission radius, and s is a power-law index, which for our model is set to 0.5 (see, e.g., Yuan et al. 2012; Guo et al. 2024). For the other parameters, we use the same values as for the single-zone model.

As seen in Fig. 5, the emission from the outer zones is several orders of magnitude smaller than that from the innermost region. This is because the synchrotron and Comptonization luminosities from RIAFs are very sensitive to their electron temperature (see Kimura et al. 2021). In the outer zones, the electron temperatures are limited by advection cooling instead of radiative cooling, resulting in lower temperatures and causing weak radiation across the relevant wavelengths. Although the outer zones may contribute more significantly in X-ray bands in situations where the free-free emission dominates (e.g., Yuan et al. 2003, for Sgr A*), it is insignificant in moderate accreting sources like NGC 4278.

4.2. Flux Normalization

The model has large parameter degeneracy when only X-ray data are explained. In order to avoid potential

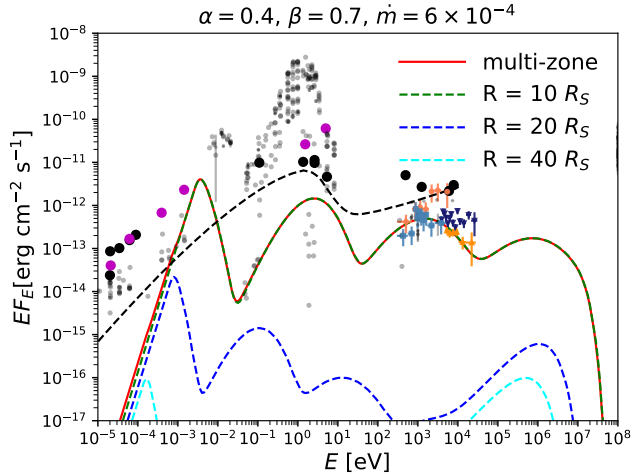


Figure 5. Multi-zone SED from different radii with $R = (10 - 40) R_S$, compared to a contribution from each radius. The archival and X-ray data points have the same legends as Fig. 3. For comparison, the LINER average SED is shown from Nemmen et al. (2009) (dashed line).

degeneracy in our choice of best-fit parameters for the RIAF SED, we attempt to normalize the SED using the sub-mm/far-IR and optical data in addition to the X-ray data obtained in this work.

However, since most of the flux in the optical band originates from the stellar population of the galaxy, we have to extract a component that is consistent with point-source emission (Bandyopadhyay et al. 2019; Nemmen et al. 2014). Similarly, the IR excess in the archival data around 0.1 eV is owed to emission from heated dust (Tang et al. 2011). Note that the radio-frequency data points would be attributed to the jet and not the RIAF.

We use the RIAF data from Bandyopadhyay et al. (2019) to normalize the optical and IR components of the SED. However, we are unable to find a model that gives a good fit for both the new X-ray data and the optical/IR component of the SED from the literature. This is not surprising because their X-ray flux, obtained from XMM-Newton observations, was higher than ours by a factor of 4. Therefore, to find the best-fit parameters for the quiescent state SED, we allow our optical flux to differ from theirs by up to the same factor (4.1). The moderate state SED is then obtained by only increasing \dot{m} to the value, for which the SED provides a fit to the moderate state NuSTAR data or active state *Swift*-XRT data. The physical explanation for this is that both states describe the same fluid flow, but the rate of accretion is greater during the active state. As a result, the ratio between the X-ray peaks is smaller than that between the optical peaks for this state, and

the peak energy of the X-ray spectrum is lowered, as one would expect from the results in the third panel of Fig. 4. Note that Nemmen et al. (2009) presents an averaged LINER SED, which appears quite different from pure RIAF SEDs commonly used in the literature. This difference is likely expected, because the data-driven SED template effectively averages over a heterogeneous population and may include substantial contributions from components beyond the RIAF itself (e.g., jets, truncated thin disks, and stellar contamination), which can wash out the characteristic spectral features of the RIAF SED model. As seen in Fig. 5, the data in the optical band from Nemmen et al. (2014) largely overshoots this averaged SED, which could be caused by the stellar contamination.

4.3. Main Results

We vary the viscosity parameter α in the range [0.03, 1], the plasma β in [10^{-3} , 10], and the accretion rate \dot{m} within the range [10^{-5} , 10^{-2}]. We find the best-fit values for α to be 0.4 and for β to be 0.7, respectively. These are typical values for the RIAF model. The best-fit value of \dot{m} is found to be 6×10^{-4} for the quiescent X-ray state and 10^{-3} for the moderate state. The best-fit parameters are listed in Table 2.

RIAFs can be sorted into one of two categories based on the magnetic topology. One of these is the magnetically arrested disk (MAD) (Narayan et al. 2003), where the magnetic stresses are comparable to those required to impede the inflow (magnetic arrest), leading to a flux-saturated, highly variable accretion. The other is the standard and normal evolution (SANE) (Narayan et al. 2012), where the magnetization is much weaker in the bulk of the flow, and the flux saturation is absent, and the accretion proceeds in the standard turbulence driven by the magnetorotational instability (Balbus & Hawley 1998). While values of β vary depending on regions, our choice of β infers the MAD-like disk, $\beta \sim 0.1 - 10$ at the disk midplane (e.g., Chael et al. 2018), while for SANE, it is usually in the range $\beta \sim 10 - 100$ (e.g., Kimura et al. 2019b). Although the plasma β itself is not enough to determine whether the flow is in the MAD or SANE, the MAD would be necessary to launch powerful jets (Tchekhovskoy et al. 2011), which is consistent with the indication of jets in NGC 4278 (Giroletti et al. 2005; Chen et al. 2026). The required jet power without protons is $\gtrsim 10^{39} - 10^{43}$ erg s $^{-1}$, depending on models, which can be comparable to or smaller than our inferred values, $\dot{M}c^2 \sim (2 - 4) \times 10^{43}$ erg s $^{-1}$.

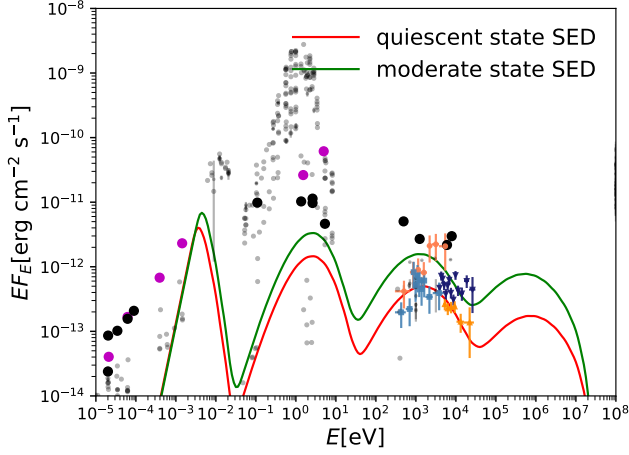


Figure 6. Best fit results for a single-zone model using a typical emission radius of $10 R_S$. The best fit parameters for the SED are listed in table 2. The archival and X-ray data points have the same legends as Fig. 3. The purple and black data points are from Nemmen et al. (2014) and Bandyopadhyay et al. (2019), respectively.

Table 2. SED parameters for the single-zone RIAF model with $R = 10 R_S$.

RIAF state	α	β	\dot{m}
quiescent state	0.4	0.7	6×10^{-4}
moderate state	0.4	0.7	10^{-3}

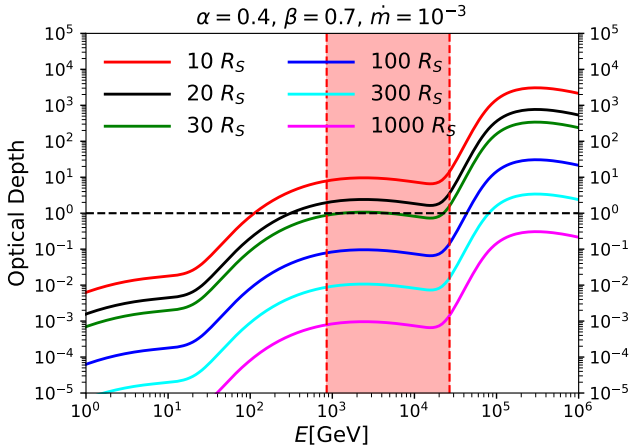


Figure 7. Two-photon annihilation optical depths for the single-zone moderate state SED at different emission radii. The red shaded region is the LHAASO energy band.

5. DISCUSSIONS

5.1. Incapability of the escape of very high-energy gamma rays from the RIAF disk

It is interesting to ask whether the RIAF model explains very high-energy gamma rays from the RIAF.

For the RIAF model to explain the LHAASO data, the source must be transparent to gamma rays in the 1–25 TeV energy range. These gamma rays primarily react with IR photons from the disk to produce electron-positron pairs. The optical depth for electron-positron pair production from the two-photon annihilation process is as follows (Murase 2022; Das et al. 2024),

$$\begin{aligned} \tau_{\gamma\gamma \rightarrow e^+e^-} &\approx \eta_{\gamma\gamma} \sigma_T R \tilde{n}_{\text{disk}} \left(\frac{\varepsilon_\gamma}{\tilde{\varepsilon}_\gamma^{e^+e^-} - \text{IR}} \right)^{\Gamma_{\text{disk}} - 1} \\ &\sim 20 \tilde{L}_{\text{disk}, 39.5} \left(\frac{\varepsilon_{\text{IR}}}{0.1 \text{ eV}} \right)^{-1} \left(\frac{R}{10 R_S} \right)^{-1} \\ &\quad \left(\frac{M_{\text{BH}}}{3 \times 10^8 M_\odot} \right)^{-1} \left(\frac{\varepsilon_\gamma}{\tilde{\varepsilon}_\gamma^{e^+e^-} - \text{IR}} \right)^{\Gamma_{\text{disk}} - 1}, \end{aligned} \quad (7)$$

where $\eta_{\gamma\gamma} \sim 0.2$ is a coefficient that is dependent on the photon index of RIAF IR emission Γ_{disk} (Svensson 1987), $\sigma_T \approx 6.65 \times 10^{-25} \text{ cm}^2$ is the Thomson cross section, $\tilde{L}_{\text{disk}} \sim 3 \times 10^{39} \text{ erg s}^{-1}$ is the differential luminosity of the disk at $\varepsilon_{\text{IR}} \sim 0.1 \text{ eV}$, M_{BH} is the black hole mass, $\sim 3 \times 10^8 M_\odot$ for our source, the characteristic gamma-ray energy interacting is $\tilde{\varepsilon}_\gamma^{e^+e^-} - \text{IR} \approx m_e^2 c^4 / \varepsilon_{\text{IR}} \simeq 2.6 \text{ TeV} (\varepsilon_{\text{IR}} / 0.1 \text{ eV})^{-1}$, and the photon index of the disk spectrum is $\Gamma_{\text{disk}} \sim 1$. This equation is consistent with the numerical results shown in Fig. 7. Setting $\tau_{\gamma\gamma \rightarrow e^+e^-} \leq 1$ in the LHAASO band to allow the gamma rays to escape gives us $R \gtrsim 30 R_S$. This disfavors the RIAF disk itself as the potential region of the LHAASO gamma-ray emission (although the attenuation could be compensated by increasing the dissipation power). We therefore conclude that the TeV gamma rays detected by LHAASO are more likely originate from outer regions, such as the jet or wind driven by the LLAGN.

A recent work from Chen et al. (2026) has demonstrated that the gamma-ray observation from LHAASO (both quiet and active states) can be explained by a jet modeled with an external inverse-Compton (EIC) scenario. They argue that the EIC process may be critical to very high-energy gamma-ray production in NGC 4278 and provides a better fit to the observed data than a synchrotron self-Compton (SSC) or leptohadronic models. The RIAF emission in this work can serve as target photons for the jet EIC process. As an alternative model, Yuan & Liu (2026) have explored the possibility of explaining the X-ray and gamma-ray states by leptohadronic radiation from a sub-relativistic wind. However, these models cannot be distinguished with current observations.

In the jet model, the gamma rays are more likely to originate from purely leptonic processes, although lep-

tohadronic processes have also been considered (Chen et al. 2026). In the wind scenario, however, the gamma rays could have a primarily hadronic origin (Yuan & Liu 2026). In either case, the gamma-ray emitting region must be sufficiently far away from the center, $R \gtrsim 30 R_S$, which is consistent with our conclusion.

5.2. Low-luminosity AGNs as hidden neutrino sources and possible connections to turbulent coronae of Seyfert galaxies

As shown in the previous subsection, TeV gamma rays cannot escape from RIAFs. However, neutrinos freely escape from RIAF disks. It has been demonstrated that RIAFs in LLAGNs are capable of accelerating protons to PeV energies, leading to the production of PeV neutrinos through hadronuclear/photohadronic processes (Kimura et al. 2015, 2019a; Kimura & Toma 2020; Kimura et al. 2021). Fig. 8 shows neutrino spectra from our RIAF models (see Kimura et al. (2019a) for computational methods). Model A corresponds to efficient acceleration with $\eta_{\text{acc}} = 10$, where η_{acc} is the acceleration efficiency defined as $t_{\text{acc}} = \eta_{\text{acc}} r_L / c$ with t_{acc} and r_L being acceleration timescale and Larmor radius, respectively. Model B uses the lower acceleration efficiency with $\eta_{\text{acc}} = 1.0 \times 10^4$. Model A and Model B are similar to those in Kimura & Toma (2020) and Kimura et al. (2021), respectively. We use the cosmic-ray injection efficiency of $\eta_{\text{CR}} = 0.01$ for both Models A and B, which is defined as $L_{\text{CR}} = \eta_{\text{CR}} \dot{M} c^2$ with L_{CR} being cosmic-ray luminosity. The power-law CR injection spectrum with spectral index of 1 is assumed for simplicity. We also stress that the turbulent RIAF model presented by Kimura et al. (2019a) and Kimura et al. (2021) describes SANE-like and MAD-like ($\beta \lesssim 0.1-10$) disks in a unified manner, in the sense that the turbulent magnetic field is parameterized by the plasma beta in the same phenomenological framework.

In Model A, cosmic-ray protons are accelerated to higher energies of ~ 100 PeV, leading to efficient $p\gamma$ interaction and higher neutrino luminosity with $E_\nu \sim 10$ PeV. On the other hand, the maximum energy of cosmic-ray protons in Model B is limited to ~ 1 PeV, where the pp channel is dominant and pion production efficiency is lower, compared to Model A, leading to weaker neutrino emission. Since the magnetic field is not strong, pion synchrotron cooling is negligible in both Models. We should note that the cosmic-ray pressure in the RIAF is close to the theoretical limit, $P_{\text{CR}}/P_{\text{th}} \sim 0.4$ and 0.5 for Models A and B, respectively. Although the proton-induced electromagnetic cascade leads to a broadband emission from keV X rays to sub-TeV gamma rays, this cascade emission is subdominant compared to the MeV

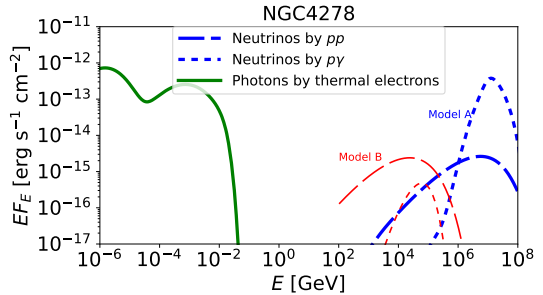


Figure 8. Neutrino spectra from our RIAF model. The solid line is the photon spectrum emitted by thermal electrons. The dotted and dashed lines are neutrino spectra by $p\gamma$ and pp interactions, respectively. The blue and red lines are for model A ($\eta_{\text{acc}} = 10$) and model B ($\eta_{\text{acc}} = 1.0 \times 10^4$), respectively (see text for the definition of η_{acc}).

gamma rays from the Comptonization process of thermal electrons (Kimura et al. 2019a).

The expected neutrino flux in our model can be comparable to the TeV gamma-ray flux detected by LHAASO, although the RIAF disk should be “hidden” in TeV gamma rays. This flux can be similar to the neutrino flux for the lepto-hadronic wind model discussed in Yuan & Liu (2026). However, their wind model assumes cosmic-ray luminosity of $L_{\text{CR}} \sim 10^{44}$ erg s $^{-1}$, which would be larger than energy budget of the system, $\dot{M} c^2 \sim 4 \times 10^{43}$ erg s $^{-1} \ll L_{\text{Edd}}$, as estimated by our X-ray emission modeling with RIAFs. In contrast, for the jet model, the gamma rays can be dominated by EIC scattering from relativistic electrons and RIAF target photons. Neutrino emission in cases where the observed gamma rays are leptonic rather than hadronic has been extensively studied in the context of jet-loud AGNs, including detailed effects of external target photons (Murase et al. 2014; Dermer et al. 2014). In such jet models, the predicted neutrino fluxes are typically lower than the observed TeV gamma-ray flux, i.e., $L_\nu \lesssim L_\gamma$. This is indeed the case for NGC 4278, and the expected neutrino flux may be 3-4 orders of magnitude lower than the TeV gamma-ray flux (see also Chen et al. 2026). Therefore, our neutrino flux can be treated as upper limits of the two-zone picture consisting of the RIAF and jet in which TeV gamma rays have a leptonic origin.

Coronal regions of radiatively efficient disks could be regarded as RIAF-like regions, and coronae of Seyfert galaxies have been proposed as the promising origin of medium-energy neutrinos in the 10-100 TeV range (Murase et al. 2020, 2026). This model predicts that NGC 1068 and NGC 4151 are among the brightest neutrino sources in the IceCube sky (Kheirandish et al. 2021; Murase et al. 2024), as well as a correlation between the neutrino and X-ray luminosities, i.e., a

$L_\nu - L_X$ relation. A similar relation is expected in the RIAF model (Kimura et al. 2019a), which tempts us to extend the $L_\nu - L_X$ relation down to lower luminosities, i.e., from Seyfert galaxies to low-luminosity AGNs.

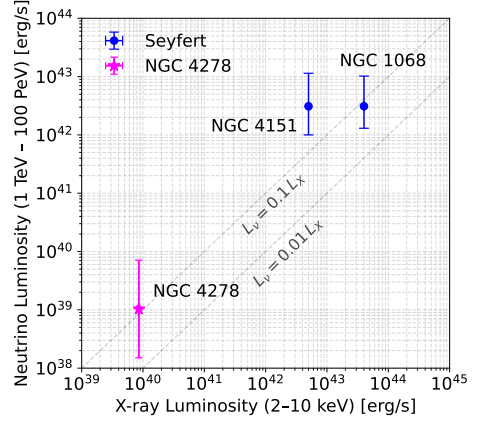
Fig. 9(a) shows a possible scaling relation between the intrinsic 2-10 keV hard X-ray luminosity and the neutrino luminosity from Seyfert galaxies. The estimation of neutrino luminosities is sensitive to the templates of neutrino spectra, and the power-law assumption is not valid in general, or at least can be misleading for the model comparison. Thus, for the neutrino luminosities of NGC 1068 and NGC 4151, we use the estimates by Carpio et al. (2026), which obtain lower values than those reported in Kun et al. (2024). Using the observed hard X-ray flux of NGC 4278 (see Section 2.1) and the rough estimation of the neutrino flux above, we show that NGC 4278 follows the same hard X-ray/neutrino correlation seen in Seyfert galaxies. Fig. 9(b) is similar to Fig. 9(a) but shows a relation between the hard X-ray and neutrino fluxes.

6. SUMMARY

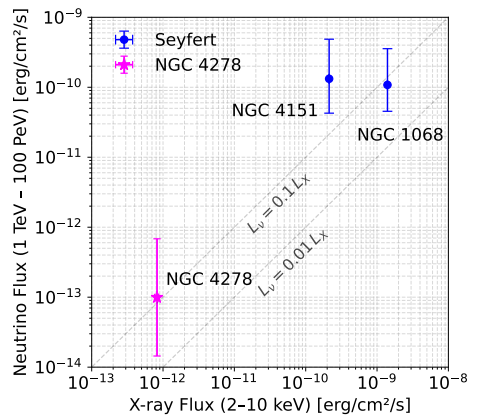
In this study, we reported recent *Swift*-XRT and NuSTAR X-ray observations for the low-luminosity active galactic nucleus (LLAGN) NGC 4278. The NuSTAR observations led to the first measurements of the hard X-ray spectrum of this source beyond 10 keV, showing a rather flat spectrum with a power-law index around 2 with no sign of a cutoff toward high energies. These observations reveal a lower-flux state compared to the LHAASO-reported active state. Flux variability by a factor of ~ 2 was observed on timescales of a month.

We interpreted the spectral variability of the X-ray emission using a radiatively inefficient accretion flow (RIAF) model. The X-ray variability can be explained by changing the accretion rate. We found the best-fit parameters for both the quiescent and moderate states. We also explored both single-zone and multi-zone models and concluded that the contribution from the outer layers is negligible in comparison to that from the innermost region. We also found that the magnetically arrested disk is favored within our RIAF model, which is consistent with the jet model for TeV gamma rays observed by LHAASO (Chen et al. 2026).

The TeV gamma rays observed in LHAASO, on the other hand, cannot be produced in the innermost region of the RIAF disk, and more likely come from outer regions ($R \gtrsim 30R_S$), such as the jet or the wind. We studied NGC 4278 as a hidden neutrino source, and discussed a possible correlation between the observed hard X-ray and the hypothetical neutrino luminosity that could ex-



(a)



(b)

Figure 9. (a) Possible scaling relation between the hard X-ray and the expected neutrino luminosities. The data from Seyfert galaxies are from Carpio et al. (2026). We highlight the caveat that no evidence for any neutrino emission from NGC 4278 has ever been reported. (b) Similar to (a), but for fluxes.

ist over many orders of magnitude in luminosity between LLAGNs and Seyfert galaxies.

ACKNOWLEDGMENTS

We thank Jose Carpio for allowing us to show the data points of neutrino luminosities. We also thank Bing Theodore Zhang for discussions. This research is supported by grants from the U.S. National Science Foundation PHY-2411860 and NASA 80NSSC25K7694. The work of K.M. was supported by the NSF Grants No. AST-2108466, No. AST-2108467, and No. 2308021. S.S.K. acknowledges support by KAKENHI Nos. 22K14028, 21H04487, 23H04899, and the Tohoku Initiative for Fostering Global Researchers for Interdisciplinary Sciences (TI-FRIS) of MEXT's Strategic Professional Development Program for Young

Researchers. This work made use of data supplied by the UK *Swift* Science Data Centre at the University of Leicester.

This research has made use of the NASA/IPAC Extragalactic Database, which is funded by the National Aeronautics and Space Administration and operated by the California Institute of Technology.

Facilities: NuSTAR, *Swift*-XRT

Software: Astropy (Astropy Collaboration et al. 2013, 2018), NumPy (van der Walt et al. 2011), Matplotlib (Hunter 2007), SciPy (Jones et al. 2001), HEASOFT (Nasa High Energy Astrophysics Science Archive Research Center (Heasarc) 2014)

REFERENCES

- Astropy Collaboration, Robitaille, T. P., Tollerud, E. J., et al. 2013, *A&A*, 558, A33, doi: [10.1051/0004-6361/201322068](https://doi.org/10.1051/0004-6361/201322068)
- Astropy Collaboration, Price-Whelan, A. M., Sipőcz, B. M., et al. 2018, *AJ*, 156, 123, doi: [10.3847/1538-3881/aabc4f](https://doi.org/10.3847/1538-3881/aabc4f)
- Balbus, S. A., & Hawley, J. F. 1998, *Rev. Mod. Phys.*, 70, 1, doi: [10.1103/RevModPhys.70.1](https://doi.org/10.1103/RevModPhys.70.1)
- Baldini, L., Ballet, J., Bastieri, D., et al. 2021, *The Astrophysical Journal Supplement Series*, 256, 13
- Bandyopadhyay, B., Xie, F.-G., Nagar, N. M., et al. 2019, *Monthly Notices of the Royal Astronomical Society*, 490, 4606, doi: [10.1093/mnras/stz2874](https://doi.org/10.1093/mnras/stz2874)
- Blandford, R. D., & Begelman, M. C. 1999, *Monthly Notices of the Royal Astronomical Society*, 303, L1, doi: [10.1046/j.1365-8711.1999.02358.x](https://doi.org/10.1046/j.1365-8711.1999.02358.x)
- Boller, T., Freyberg, M. J., Trümper, J., et al. 2016, *aap*, 588, A103, doi: [10.1051/0004-6361/201525648](https://doi.org/10.1051/0004-6361/201525648)
- Bronzini, E., Grandi, P., Torresi, E., & Buson, S. 2024, *ApJL*, 977, L16, doi: [10.3847/2041-8213/ad93cf](https://doi.org/10.3847/2041-8213/ad93cf)
- Burrows, D. N., Hill, J. E., Nousek, J. A., et al. 2005, *SSRv*, 120, 165, doi: [10.1007/s11214-005-5097-2](https://doi.org/10.1007/s11214-005-5097-2)
- Cao, Z., Aharonian, F., An, Q., et al. 2024a, *ApJS*, 271, 25, doi: [10.3847/1538-4365/acfd29](https://doi.org/10.3847/1538-4365/acfd29)
- Cao, Z., Aharonian, F., Axikegu, et al. 2024b, *ApJL*, 971, L45, doi: [10.3847/2041-8213/ad5e6d](https://doi.org/10.3847/2041-8213/ad5e6d)
- Carpio, J. A., Kheirandish, A., & Murase, K. 2026, to be submitted
- Chael, A., Rowan, M. E., Narayan, R., Johnson, M. D., & Sironi, L. 2018, *Mon. Not. Roy. Astron. Soc.*, 478, 5209, doi: [10.1093/mnras/sty1261](https://doi.org/10.1093/mnras/sty1261)
- Chen, S., Das, A., Zhang, B. T., et al. 2026, Physical origin of very-high-energy gamma rays from the low-luminosity active galactic nucleus NGC 4278 and implications for neutrino observations. <https://arxiv.org/abs/2601.23242>
- Condon, J. J., Cotton, W. D., Greisen, E. W., et al. 1998, *AJ*, 115, 1693, doi: [10.1086/300337](https://doi.org/10.1086/300337)
- Das, A., Zhang, B. T., & Murase, K. 2024, *The Astrophysical Journal*, 972, 44, doi: [10.3847/1538-4357/ad5a04](https://doi.org/10.3847/1538-4357/ad5a04)
- Dermer, C. D., Murase, K., & Inoue, Y. 2014, *JHEAp*, 3-4, 29, doi: [10.1016/j.jheap.2014.09.001](https://doi.org/10.1016/j.jheap.2014.09.001)
- Dixon, R. S. 1970, *ApJS*, 20, 1, doi: [10.1086/190216](https://doi.org/10.1086/190216)
- Gehrels, N., Chincarini, G., Giommi, P., et al. 2004, *ApJ*, 611, 1005, doi: [10.1086/422091](https://doi.org/10.1086/422091)
- Giroletti, M., Taylor, G. B., & Giovannini, G. 2005, *ApJ*, 622, 178, doi: [10.1086/427898](https://doi.org/10.1086/427898)
- Gregory, P. C., Scott, W. K., Douglas, K., & Condon, J. J. 1996, *ApJS*, 103, 427, doi: [10.1086/192282](https://doi.org/10.1086/192282)
- Guo, M., Stone, J. M., Quataert, E., & Kim, C.-G. 2024, *Astrophys. J.*, 973, 141, doi: [10.3847/1538-4357/ad5fe7](https://doi.org/10.3847/1538-4357/ad5fe7)
- H. E. S. S. Collaboration, Aharonian, F., Ait Benkhali, F., et al. 2022, *Science*, 376, 77, doi: [10.1126/science.abn0567](https://doi.org/10.1126/science.abn0567)
- Harrison, F. A., Craig, W. W., Christensen, F. E., et al. 2013, *ApJ*, 770, 103, doi: [10.1088/0004-637x/770/2/103](https://doi.org/10.1088/0004-637x/770/2/103)
- Healey, S. E., Romani, R. W., Taylor, G. B., et al. 2007, *ApJS*, 171, 61, doi: [10.1086/513742](https://doi.org/10.1086/513742)
- Hunter, J. D. 2007, *Computing in Science and Engineering*, 9, 90, doi: [10.1109/MCSE.2007.55](https://doi.org/10.1109/MCSE.2007.55)
- Jackson, N., Battye, R. A., Browne, I. W. A., et al. 2007, *MNRAS*, 376, 371, doi: [10.1111/j.1365-2966.2007.11442.x](https://doi.org/10.1111/j.1365-2966.2007.11442.x)
- Joint Iras Science, W. G. 1994, *VizieR Online Data Catalog*, 2125, 0
- Jones, E., Oliphant, T., Peterson, P., et al. 2001, *SciPy: Open source scientific tools for Python*. <http://www.scipy.org/>
- Kheirandish, A., Murase, K., & Kimura, S. S. 2021, *Astrophys. J.*, 922, 45, doi: [10.3847/1538-4357/ac1c77](https://doi.org/10.3847/1538-4357/ac1c77)
- Kimura, S. S., Kashiyama, K., & Hotokezaka, K. 2021, *Astrophys. J. Lett.*, 922, L15, doi: [10.3847/2041-8213/ac35dc](https://doi.org/10.3847/2041-8213/ac35dc)
- Kimura, S. S., Murase, K., & Mészáros, P. 2019a, *Phys. Rev. D*, 100, 083014, doi: [10.1103/PhysRevD.100.083014](https://doi.org/10.1103/PhysRevD.100.083014)
- Kimura, S. S., Murase, K., & Mészáros, P. 2021, *Nature Communications*, 12, 5615, doi: [10.1038/s41467-021-25111-7](https://doi.org/10.1038/s41467-021-25111-7)
- Kimura, S. S., Murase, K., & Toma, K. 2015, *Astrophys. J.*, 806, 159, doi: [10.1088/0004-637X/806/2/159](https://doi.org/10.1088/0004-637X/806/2/159)
- Kimura, S. S., & Toma, K. 2020, *Astrophys. J.*, 905, 178, doi: [10.3847/1538-4357/abc343](https://doi.org/10.3847/1538-4357/abc343)

- Kimura, S. S., Tomida, K., & Murase, K. 2019b, *Mon. Not. Roy. Astron. Soc.*, 485, 163, doi: [10.1093/mnras/stz329](https://doi.org/10.1093/mnras/stz329)
- Kun, E., Bartos, I., Becker Tjus, J., et al. 2024, arXiv e-prints, arXiv:2404.06867, doi: [10.48550/arXiv.2404.06867](https://doi.org/10.48550/arXiv.2404.06867)
- Mahadevan, R. 1997, *Astrophys. J.*, 477, 585, doi: [10.1086/303727](https://doi.org/10.1086/303727)
- Moshir, M., & et al. 1990, in *IRAS Faint Source Catalogue, version 2.0 (1990)*, 0
- Murase, K. 2022, *ApJL*, 941, L17, doi: [10.3847/2041-8213/aca53c](https://doi.org/10.3847/2041-8213/aca53c)
- Murase, K., Inoue, Y., & Dermer, C. D. 2014, *Phys. Rev. D*, 90, 023007, doi: [10.1103/PhysRevD.90.023007](https://doi.org/10.1103/PhysRevD.90.023007)
- Murase, K., Karwin, C. M., Kimura, S. S., Ajello, M., & Buson, S. 2024, *Astrophys. J. Lett.*, 961, L34, doi: [10.3847/2041-8213/ad19c5](https://doi.org/10.3847/2041-8213/ad19c5)
- Murase, K., Kimura, S. S., & Meszaros, P. 2020, *Phys. Rev. Lett.*, 125, 011101, doi: [10.1103/PhysRevLett.125.011101](https://doi.org/10.1103/PhysRevLett.125.011101)
- Murase, K., Kimura, S. S., Mukhopadhyay, M., & Bhattacharya, M. 2026. <https://arxiv.org/abs/2602.20145>
- Myers, S. T., Jackson, N. J., Browne, I. W. A., et al. 2003, *MNRAS*, 341, 1, doi: [10.1046/j.1365-8711.2003.06256.x](https://doi.org/10.1046/j.1365-8711.2003.06256.x)
- Narayan, R., Igumenshchev, I. V., & Abramowicz, M. A. 2003, *Publications of the Astronomical Society of Japan*, 55, L69, doi: [10.1093/pasj/55.6.L69](https://doi.org/10.1093/pasj/55.6.L69)
- Narayan, R., Sadowski, A., Penna, R. F., & Kulkarni, A. K. 2012, *Monthly Notices of the Royal Astronomical Society*, 426, 3241, doi: [10.1111/j.1365-2966.2012.22002.x](https://doi.org/10.1111/j.1365-2966.2012.22002.x)
- Narayan, R., & Yi, I. 1994, *ApJL*, 428, L13, doi: [10.1086/187381](https://doi.org/10.1086/187381)
- Nasa High Energy Astrophysics Science Archive Research Center (Heasarc). 2014, *HEASoft: Unified Release of FTOOLS and XANADU*, *Astrophysics Source Code Library*, record ascl:1408.004. <http://ascl.net/1408.004>
- Nemmen, R. S., Storchi-Bergmann, T., & Eracleous, M. 2014, *Monthly Notices of the Royal Astronomical Society*, 438, 2804, doi: [10.1093/mnras/stt2388](https://doi.org/10.1093/mnras/stt2388)
- Nemmen, R. S., Storchi-Bergmann, T., Eracleous, M., & Yuan, F. 2009, *Proceedings of the International Astronomical Union*, 5, 313–318, doi: [10.1017/S1743921310006538](https://doi.org/10.1017/S1743921310006538)
- Pellegrini, S., Wang, J., Fabbiano, G., et al. 2012, *ApJ*, 758, 94, doi: [10.1088/0004-637X/758/2/94](https://doi.org/10.1088/0004-637X/758/2/94)
- Pesce, D. W., Palumbo, D. C. M., Narayan, R., et al. 2021, *Astrophys. J.*, 923, 260, doi: [10.3847/1538-4357/ac2eb5](https://doi.org/10.3847/1538-4357/ac2eb5)
- Stratta, G., Capalbi, M., Giommi, P., et al. 2011, arXiv e-prints, arXiv:1103.0749, doi: [10.48550/arXiv.1103.0749](https://doi.org/10.48550/arXiv.1103.0749)
- Svensson, R. 1987, *Mon. Not. Roy. Astron. Soc.*, 227, 403
- Tang, Y., Gu, Q., Zhang, S., & Tang, B. 2011, *Monthly Notices of the Royal Astronomical Society*, 414, 1827, doi: [10.1111/j.1365-2966.2011.18267.x](https://doi.org/10.1111/j.1365-2966.2011.18267.x)
- Tchekhovskoy, A., Narayan, R., & McKinney, J. C. 2011, *MNRAS*, 418, L79, doi: [10.1111/j.1745-3933.2011.01147.x](https://doi.org/10.1111/j.1745-3933.2011.01147.x)
- Tremblay, S. E., Taylor, G. B., Ortiz, A. A., et al. 2016, *MNRAS*, 459, 820, doi: [10.1093/mnras/stw592](https://doi.org/10.1093/mnras/stw592)
- van der Walt, S., Colbert, S. C., & Varoquaux, G. 2011, *Computing in Science Engineering*, 13, 22, doi: [10.1109/MCSE.2011.37](https://doi.org/10.1109/MCSE.2011.37)
- Vaughan, S., Edelson, R., Warwick, R. S., & Uttley, P. 2003, *MNRAS*, 345, 1271, doi: [10.1046/j.1365-2966.2003.07042.x](https://doi.org/10.1046/j.1365-2966.2003.07042.x)
- Voges, W., Aschenbach, B., Boller, T., et al. 1999, *A&A*, 349, 389
- Wang, T.-G., & Zhang, X.-G. 2003, *MNRAS*, 340, 793, doi: [10.1046/j.1365-8711.2003.06336.x](https://doi.org/10.1046/j.1365-8711.2003.06336.x)
- White, R. L., & Becker, R. H. 1992, *ApJS*, 79, 331, doi: [10.1086/191656](https://doi.org/10.1086/191656)
- White, R. L., Becker, R. H., Helfand, D. J., & Gregg, M. D. 1997, *ApJ*, 475, 479
- Willingale, R., Starling, R. L. C., Beardmore, A. P., Tanvir, N. R., & O'Brien, P. T. 2013, *MNRAS*, 431, 394, doi: [10.1093/mnras/stt175](https://doi.org/10.1093/mnras/stt175)
- Wright, E. L., Eisenhardt, P. R. M., Mainzer, A. K., et al. 2010, *AJ*, 140, 1868, doi: [10.1088/0004-6256/140/6/1868](https://doi.org/10.1088/0004-6256/140/6/1868)
- Younes, G., Porquet, D., Sabra, B., et al. 2010, *A&A*, 517, A33, doi: [10.1051/0004-6361/201014371](https://doi.org/10.1051/0004-6361/201014371)
- Yuan, C., & Liu, R.-Y. 2026, *TeV Gamma-Rays from the Low-Luminosity Active Galactic Nucleus NGC 4278: Implications for the Diffuse Neutrino Background*. <https://arxiv.org/abs/2601.21411>
- Yuan, F., Quataert, E., & Narayan, R. 2003, *Astrophys. J.*, 598, 301, doi: [10.1086/378716](https://doi.org/10.1086/378716)
- Yuan, F., Wu, M., & Bu, D. 2012, *The Astrophysical Journal*, 761, 129, doi: [10.1088/0004-637X/761/2/129](https://doi.org/10.1088/0004-637X/761/2/129)